Guided Wave Damage Characterisation in Beams Utilising Probabilistic Optimisation

C.T. Ng[1,2], M. Veidt*[1] and H.F. Lam[3]

[1] School of Engineering, The University of Queensland, Brisbane, Qld, 4072
[2] Cooperative Research Centre for Advanced Composite Structures Ltd, Fishermans Bend, Vic, 3201
[3] Department of Building and Construction, City University of Hong Kong, 83 Tat Chee Avenue, Kowloon, Hong Kong

Corresponding author
Tel.: +61 7 3365 3621
Fax: +61 7 3365 4799
Email address: m.veidt@uq.edu.au

Total 36 pages: 18 text, including this page + 14 figure pages + 4 table pages

Guided Wave Damage Characterisation in Beams Utilising Probabilistic Optimisation

C.T. Ng[1,2], M. Veidt*[1] and H.F. Lam[3]

[1] School of Engineering, The University of Queensland, Brisbane, Qld, 4072
[2] Cooperative Research Centre for Advanced Composite Structures Ltd, Fishermans Bend, Vic, 3201
[3] Department of Building and Construction, City University of Hong Kong, 83 Tat Chee Avenue, Kowloon, Hong Kong

Abstract

This paper introduces a probabilistic optimisation approach to the characterisation of damage in beams using guided waves. The proposed methodology not only determines multivariate damage characteristics, but also quantifies the associated uncertainties of the predicted values, thus providing essential information for making decisions on necessary remedial work. The damage location, length and depth and Young's modulus of the material are treated as unknown model parameters. Characterisation is achieved by applying a two-stage optimisation process that uses simulated annealing to guarantee that the solution is close to the global optimum, followed by a standard simplex search method that maximises the probability density function of a damage scenario conditional on the measurement data. The proposed methodology is applied to characterise laminar damage and is verified through a comprehensive series of numerical case studies that use spectral finite element wave propagation modelling with the consideration of both measurement noise and material uncertainty. The methodology is accurate and robust, and successfully detects damage even when the fault is close to the end of the beam and its length and depth are small. The particularly valuable feature of the proposed methodology is its ability to quantify the uncertainties associated with the damage characterisation results. The effects of measurement noise level, damage location, length and depth on the uncertainties in damage detection results are studied and discussed in detail.

Keywords: Guided Wave, Beam Damage Characterisation, Bayesian Statistical Framework, Probabilistic Optimisation.

1 Introduction

The detection of damage in one-dimensional structures such as beams and pipes using ultrasonics has been studied for a very long time. Conventional A- or C-scan ultrasonic techniques require measurements in the close vicinity of the damage, which is usually not feasible for large structures due to high costs and poor accessibility. Low-frequency damage detection methods that utilise natural frequencies [1], modeshapes [2-4] or time domain dynamic responses [5-6] are able to monitor the health of entire structures, but rely on low-frequency characteristics that are insensitive to small damage and usually return large errors for higher frequencies. A comprehensive review of these methods is given in [7].

Guided wave-based damage characterisation methodologies have been widely reported to be capable of monitoring large areas of structures and also being efficient and sensitive in detecting fatigue cracks in metallic structures, disbonds and delaminations in composite structures, and for the assessment of structural repairs [8-9]. For beam structures, Jiang *et al*. [10] used the time-of-flight difference between the healthy and damaged condition of a beam to identify the damage location, and then identified the damage severity from a power consumption metric defined in the frequency domain. Krawczuk [11] used a genetic algorithm gradient technique to identify a crack in a beam, in which the crack was modelled as a dimensionless spring. Li *et al*. [12] employed continuous wavelet transform to extract the reflected and transmitted flexural waves from a crack for damage identification, and Liew and Veidt [13] applied wavelet decomposition and artificial neural network based pattern recognition techniques to characterise laminar damage in beam structures.

For non-model based approaches such as that of Jiang *et al*. [10], reliable baseline subtraction is an essential requirement, which entails the accurate extraction of changes due to damage by analysing the pre- and post-damage time signals. It has been shown that reliable baseline subtraction is a difficult process for guided waves, and that even small changes in environmental conditions (e.g., temperature) may result in large errors [14]. Model-based techniques, in contrast, involve the use of an analytical or numerical model that describes the propagation of the interrogating wave and its reflection and transmission at interfaces and boundaries.

Optimisation is a powerful technique in engineering application such as structural design, system identification and damage characterisation. In the literature different types of optimisation algorithm have been developed to determine the global optimum such as genetic algorithms, evolution strategies and simulated annealing [15]. Some methods hybridise two different optimisation algorithms to increase the efficiency. A genetic simulated annealing method [16], which combines genetic algorithm and simulated annealing to locate the global optimum, has been applied to

flowshop scheduling problems. A hybrid genetic algorithm [17] has been developed and applied to mixed-discrete nonlinear design optimisation problems, where the genetic algorithm is used to determine the feasible region containing the global optimum point. The hybrid negative sub-gradient method is then used to find the global optimal. A hybrid optimisation approach combining evolution strategies and a gradient based method [18] has been employed in structural model updating problems.

This paper systematically investigates the application of a model-based probabilistic damage characterisation methodology to identify laminar damage in beam structures. An important advantage of the proposed methodology over existing methods is the Bayesian statistical framework [19] that is adopted to calculate the probability density functions (PDF) of the predicted damage characteristics. Such calculations allow the quantification of the uncertainties associated with damage detection results, information that is essential for making decisions about necessary remedial work. Another essential feature of the Bayesian statistical framework is that, if required, engineering judgment can be incorporated into the damage characterisation process to reduce the uncertainty of the results. The proposed methodology converts the damage detection problem into an optimisation problem in which the probability density function of the damage scenario is maximised conditional on the set of measured data. The objective function that is formulated in the proposed methodology is highly nonlinear, which implies that the optimisation problem may have many local optimal solutions. Traditional deterministic numerical optimisation algorithms will easily become trapped by those local minima, and thus to solve this problem a two-stage optimisation process is proposed. In the first stage, a probabilistic optimisation algorithm is employed to identify a solution that is close to the global optimal solution. In the second stage, a deterministic optimisation algorithm is used to accurately determine the global optimum.

The organisation of the paper is as follows. The proposed probabilistic methodology is presented in Section 2, along with an explanation of the fundamentals of the spectral finite element modelling of guided waves in damaged beams and the Bayesian statistical framework for quantifying the uncertainty of damage characterisation results. In Section 3, the performance of the methodology in detecting and characterising laminar damage in beams is illustrated by a series of comprehensive numerical cases studies. The section also includes investigations on the effects of different levels of measurement noise and interference of boundary reflections and scattered waves on the damage characterisation results. Conclusions are presented in Section 4.

2 Methodology

The basic concepts of wave propagation modelling in damaged beams through spectral finite element analysis are presented first. A one-dimensional spectral finite element is introduced to describe the propagation of a longitudinal wave and used to model step damage in a beam. In the second sub-section, a probabilistic approach is presented that enables the calculation of multivariate damage characteristics and the corresponding confidence levels.

2.1 Spectral finite element modelling of guided wave propagation in damaged beams

2.1.1 Spectral finite element model

A frequency domain spectral finite element [20-21] with length L_j is shown in Figure 1. The element contains two nodes each with one longitudinal degree of freedom $\hat{u}_\alpha$ and $\hat{u}_\beta$, respectively. The longitudinal wave motion is governed by elementary wave propagation theory for longitudinal waves in a linear elastic material.

$$\frac{\partial^2 u}{\partial x^2} = \frac{1}{c^2}\frac{\partial^2 u}{\partial t^2}, \tag{1}$$

where $u = u(x,t)$ is the longitudinal displacement and $c = \sqrt{E/\rho}$ is the speed of the fundamental longitudinal wave mode in a material with Young's modulus E and density ρ. The solution is assumed to have the spectral representation

$$u(x,t) = \sum_{n=1}^{N} \hat{u}(x,\omega_n) e^{-i\omega_n t}, \tag{2}$$

where i is the imaginary unit, ω_n is the circular frequency and the summation is carried out up to the Nyquist frequency ω_N. By substituting Equation (2) into (1), the governing equation is transformed from time domain to frequency domain for the discrete frequency component ω_n.

$$c^2 \frac{\partial^2 \hat{u}}{\partial x^2} + \omega_n^2 \hat{u} = 0. \tag{3}$$

The transformation changes the governing equation from a partial differential equation to a set of ordinary differential equations. The general longitudinal displacement in frequency domain is written as

$$\hat{u}(x,\omega_n) = C_\alpha e^{-ik_n x} + C_\beta e^{-ik_n (L_j - x)}, \tag{4}$$

where $k_n = \omega_n \sqrt{\rho / E}$ is the wavenumber and C_α and C_β are unknown coefficients that can be expressed in terms of the nodal displacements as

$$\begin{Bmatrix} \hat{u}_\alpha \\ \hat{u}_\beta \end{Bmatrix} = \begin{bmatrix} 1 & e^{-ik_n L_j} \\ e^{-ik_n L_j} & 1 \end{bmatrix} \begin{Bmatrix} C_\alpha \\ C_\beta \end{Bmatrix} = \mathbf{T}_1 \begin{Bmatrix} C_\alpha \\ C_\beta \end{Bmatrix}, \tag{5}$$

where $\hat{u}_\alpha$ and $\hat{u}_\beta$ are the longitudinal displacements in frequency domain at the left- and right-hand side node of the element, respectively. The forces in the frequency domain at the nodes are

$$\hat{F}_\alpha = -EA_j \frac{\partial \hat{u}_\alpha}{\partial x}, \qquad \hat{F}_\beta = EA_j \frac{\partial \hat{u}_\beta}{\partial x}, \tag{6}$$

where A_j is the cross-sectional area. The forces can be related to the unknown coefficients C_α and C_β as

$$\begin{Bmatrix} \hat{F}_\alpha \\ \hat{F}_\beta \end{Bmatrix} = ikEA \begin{bmatrix} 1 & -e^{-ik_n L_j} \\ -e^{-ik_n L_j} & 1 \end{bmatrix} \begin{Bmatrix} C_\alpha \\ C_\beta \end{Bmatrix} = \mathbf{T}_2 \begin{Bmatrix} C_\alpha \\ C_\beta \end{Bmatrix}. \tag{7}$$

Thus, the relation between the nodal forces and the nodal displacements is given as

$$\begin{Bmatrix} \hat{F}_\alpha \\ \hat{F}_\beta \end{Bmatrix} = \mathbf{T}_2 \mathbf{T}_1^{-1} \begin{Bmatrix} \hat{u}_\alpha \\ \hat{u}_\beta \end{Bmatrix} = \mathbf{K}_{\omega_n} \begin{Bmatrix} \hat{u}_\alpha \\ \hat{u}_\beta \end{Bmatrix}, \tag{8}$$

where $\mathbf{K}_{\omega_n}$ is the dynamic stiffness matrix of the spectral element at the frequency ω_n. The displacement at any location within the element is calculated using the shape function and the nodal values [20] as

$$\hat{u}(x, \omega_n) = \left(\frac{\sin k_n (L_j - x)}{\sin k_n L_j} \right) \hat{u}_\alpha + \left(\frac{\sin k_n x}{\sin k_n L_j} \right) \hat{u}_\beta \quad \text{for} \quad 0 < x < L_j. \tag{9}$$

A special feature of the spectral finite element method is that for short observation times the beam can be considered to be semi-infinite, and a so-called throw-off element can be introduced that has only a single node and is a conduit that describes waves propagating away from the system boundary. The dynamic stiffness of the throw-off element for a longitudinal wave at frequency ω_n [20] is

$$K_{\omega_n}^{0} = ik_n EA_j. \tag{10}$$

2.1.2 Modelling of step damage

Three spectral finite elements and one throw-off element are used to model a semi-infinite beam with laminar damage (see Figure 2). The step damage is simulated by reducing the cross-sectional area of element EL2, $A_2 = b(h-d)$. The cross-sectional areas of the other elements are $A_j = bh$ (j = 0, 1 and 3), where b and h are the width and height of the beam, respectively, and d is the depth of the step damage. The damage location and length are parameterised by the length of EL1 (L_1) and EL2 (L_2), respectively. In addition, it is assumed that there exists some uncertainty related to the Young's modulus of the material. Thus the system parameters considered in the probabilistic damage characterisation are

$$\mathbf{è} = \{L_1, L_2, d, E\}^T . \tag{11}$$

2.2 Probabilistic damage characterisation approach

2.2.1 Calculation of posterior probability density functions

The proposed probabilistic methodology employs the Bayesian statistical framework [19] to determine the uncertain model parameters of the damaged beam. This method not only identifies the optimal values of the damage characteristics and the Young's modulus of the material, but also calculates the posterior (updated) probability density function (PDF) of the uncertain model parameters based on a given set of measured guided wave responses D, and can thus quantify the uncertainties associated with the identified model parameters. The uncertain parameter vector $\mathbf{á} = \{\mathbf{è}^T, \sigma\}^T \in S(\mathbf{á})$ is updated, where $\mathbf{è}$ contains the damage location (L_1), length (L_2), depth (d) and Young's modulus E, as shown in Equation (11). σ is the prediction error of the guided wave response and $S(\mathbf{á})$ is a set of possible parameter values for $\mathbf{á}$.

Using Bayes' theorem, the posterior PDF of the uncertain parameter vector $\mathbf{á}$, conditional on a given set of measured guided wave responses D and the class of the damaged beam model M, can be expressed as

$$p(\mathbf{á} \mid D, M) = \frac{p(D \mid \mathbf{á}, M)\, p(\mathbf{á} \mid M)}{p(D \mid M)}, \tag{12}$$

where $p(\mathbf{á} \mid M) = \pi(\mathbf{á})$ is the prior (initial) PDF of $\mathbf{á}$ which allows the inclusion

of engineering judgment about the plausibility of the values of $\boldsymbol{\alpha}$. It can be chosen as a smooth, slowly varying PDF, which is mathematically convenient and roughly reflects the engineer's judgment regarding the relative plausibility of different values of the parameter vector $\boldsymbol{\alpha}$. The PDF of the set of measured guided wave responses D conditional on the model class M is calculated as [19]

$$p(D \mid M) = \int_{S(\boldsymbol{\alpha})} p(D \mid \boldsymbol{\alpha}, M)\, p(\boldsymbol{\alpha} \mid M)\, d\boldsymbol{\alpha} = \tau^{-1}, \tag{13}$$

where τ is a normalising constant such that the expression on the left-hand side of Equation (12) is equal to unity. Equation (12) can then be expressed as

$$p(\boldsymbol{\alpha} \mid D, M) = \tau\, p(D \mid \boldsymbol{\alpha}, M)\, \pi(\boldsymbol{\alpha}), \tag{14}$$

where $p(D \mid \boldsymbol{\alpha}, M)$ is the contribution of the measured guided wave signal and is given by [19]

$$p(D \mid \boldsymbol{\alpha}, M) = \frac{1}{\left(\sqrt{2\pi}\sigma\right)^{N_t N_o}} \exp\left[-\frac{1}{2\sigma^2} \sum_{t=1}^{N_t} \left\| u_m(t) - u(t;\boldsymbol{\theta}) \right\|^2 \right], \tag{15}$$

where N_t and N_o are the number of measured time steps and the number of measurement points, respectively. $u_m(t)$ is the measured guided wave response at the t-th time step, and $u(t;\boldsymbol{\theta})$ is the calculated guided wave response based on the model class M for a given set of uncertain parameters $\boldsymbol{\theta}$. $\|\cdot\|$ denotes the standard Euclidean norm of the second kind.

The posterior PDF of the uncertain parameters $\boldsymbol{\theta}$ can be obtained from

$$p(\boldsymbol{\theta} \mid D, M) = \int_0^\infty p(\boldsymbol{\alpha} \mid D, M)\, d\sigma = \int_0^\infty \tau\, p(D \mid \boldsymbol{\alpha}, M)\, \pi(\boldsymbol{\alpha})\, d\sigma . \tag{16}$$

As the measured guided wave response usually contains a large number of data points, Equation (16) can be evaluated using an asymptotic approximation according to [22]

$$p(\boldsymbol{\theta} \mid D, M) = \tau_1 J(\boldsymbol{\theta})^{-N_J}\, \pi(\boldsymbol{\theta}, \hat{\sigma}(\boldsymbol{\theta})), \tag{17}$$

where τ_1 is another normalising constant and $N_J = (N_t N_o - 1)/2$. $J(\boldsymbol{\theta})$ quantifies the correlation between the measured and simulated guided wave response data, and is defined as

$$J(\boldsymbol{\theta}) = \frac{1}{N_t N_o} \sum_{t=1}^{N_t} \left\| u_m(t) - u(t;\boldsymbol{\theta}) \right\|^2 = \hat{\sigma}^2(\boldsymbol{\theta}), \tag{18}$$

where $\hat{\sigma}^2(\grave{\mathbf{e}})$ is the optimal variance in the prediction error model. It should be noted that for a large number of measured data points N_t, the relative posterior probability for a component of the system parameter vector $\grave{\mathbf{e}}$ is very sensitive to the values of the corresponding component in $J(\grave{\mathbf{e}})$, and there is a finite number of optimal points $\hat{\grave{\mathbf{e}}}^{(q)}$, $q = 1,...,Q$ that satisfies

$$J\left(\hat{\grave{\mathbf{e}}}^{(q)}\right) = \min_{\grave{\mathbf{e}} \in S(\grave{\mathbf{e}})} J(\grave{\mathbf{e}}) = \hat{\sigma}^2 . \tag{19}$$

The posterior PDF of the system parameter vector $\grave{\mathbf{e}}$ for the given D and M can be approximated by a weighted sum of Gaussian distributions centred at the Q optimal points [6,19,23,24].

$$p(\grave{\mathbf{e}} \mid D, M) \approx \sum_{q=1}^{Q} w_q \Gamma\left(\hat{\grave{\mathbf{e}}}^{(q)}, \mathbf{H}_N^{-1}\left(\hat{\grave{\mathbf{e}}}^{(q)}\right)\right), \tag{20}$$

where $\Gamma(\varepsilon, \Sigma)$ denotes a multivariate Gaussian distribution with mean ε and covariance matrix Σ. $\mathbf{H}_N^{-1}\left(\hat{\grave{\mathbf{e}}}^{(q)}\right)$ is the inverse of the Hessian matrix of the function $g(\grave{\mathbf{e}}) = N_J \ln J(\grave{\mathbf{e}})$ evaluated at the optimal values $\hat{\grave{\mathbf{e}}}^{(q)}$, $q = 1,...,Q$. The weighting coefficients w_q are defined as

$$w_q = \frac{w_q'}{\sum_{q=1}^{Q} w'}, \text{ where } w_q' = \pi\left(\hat{\grave{\mathbf{e}}}^{(q)}\right)\left|\mathbf{H}_N\left(\hat{\grave{\mathbf{e}}}^{(q)}\right)\right|^{-\frac{1}{2}}. \tag{21}$$

2.2.2 Global optimisation strategy

In the proposed probabilistic methodology, the probability density function in Equation (14) is maximised to identify the most 'plausible' damage scenario based on a given set of measured guided wave responses. For a non-informative prior PDF, no prior information is assumed and the results depend only on the measured data, maximising the PDF in Equation (14) is equivalent to minimising the $J(\grave{\mathbf{e}})$ function in Equation (18), which represents the discrepancy between the measured and simulated guided wave responses. It is clear from the formulation that $J(\grave{\mathbf{e}})$ is highly nonlinear, which implies that there are many local optimal solutions in the

parameter space of interest. Figure 3 shows an example of the search space of $J(\boldsymbol{\theta})$ as a function of the damage location L_1 and the damage length L_2. The true values of the damage depth d and the Young's modulus E are used to plot this figure. The $J(\boldsymbol{\theta})$ function in the figure is normalised such that the maximum is equal to unity. The global optimal point is at L_1 = 1400 mm and L_2 = 10 mm. Figure 3 clearly shows that there are several local optimal points in the close neighbourhood of the global optimum. In this situation, the development of a robust and effective optimisation scheme is a very challenging task, because traditional deterministic numerical optimisation algorithms, such as the gradient-based optimisation methods, are easily trapped by the local optimal solutions. Stochastic optimisation methods [15] are promising techniques in exploring 'important' regions in the parameter space where the objective function is of high value. However, such methods usually require many iterative steps to identify the global optimal solution. In the proposed methodology, a stochastic optimisation algorithm, namely simulated annealing (SA) [25], is employed to identify a solution that is close to the global optimum. This solution is then employed as the initial trial for a simplex search method [26] that accurately determines the global optimal solution.

As the name implies, SA adopts the principle of annealing from materials science. It is based on the fact that certain material alloys have multiple stable states with different molecular distributions and energy levels. In the annealing process, an alloy is initially heated up to a temperature at which all particles are randomly distributed in the liquid phase. The temperature is then slowly decreased until the material solidifies. If the temperature is reduced at a sufficiently slow rate, the annealing process always guarantees that the alloy reaches its global minimum energy state.

The proposed SA procedure begins by generating a set of N_T trial states of the cost function J_l, $l = 1,...,N_T$ from a random selection of initial uncertain parameters $\boldsymbol{\theta}$. A small change in the cost function value J_l' is then generated by a small random change in the uncertain parameters $\boldsymbol{\theta}$. The new set of uncertain parameters $\boldsymbol{\theta}$ is accepted based on the acceptance probability *p*, which is defined as

$$p = \begin{cases} 1 & \text{if } \Delta E < 0 \\ e^{-\frac{\Delta E}{T}} & \text{if } \Delta E > 0 \end{cases}, \tag{22}$$

where $\Delta E = J_l' - J_l$. Thus, J_l' causing $\Delta E < 0$ is always accepted, whereas J_l' causing $\Delta E > 0$ is only accepted according to the probability given by $p = e^{-\Delta E/T}$, where T is the 'annealing temperature'. There is a high probability that the change in the uncertain parameters will be accepted when T is large, and vice versa. Thus,

SA may accept changes in the uncertain parameters that increase the value of the cost function, which helps to avoid the solution becoming trapped by the local minima. When J_l' is accepted, $J_l = J_l'$ and T is reduced, which decreases the probability p. Here, N_T = 20 and the 'temperature' reduction rate is 0.5, which means that T in the subsequent optimisation step is half the value that it is in the previous step. The SA is terminated once a certain level of convergence of the uncertain parameters is achieved or after a certain run-time limit is reached. Further details on the SA algorithm can be found in [27].

A simplex search method [26] is then applied to accurately locate the global optimal point by treating the solution from the SA as the initial trial.

3 Numerical Case Studies

The aim of the numerical case studies is to systematically investigate the robustness of the proposed probabilistic methodology to characterise laminar damage in beams. The test system consists of a 2m long aluminium beam with a width b, height h, Young's modulus E and density ρ of 12 mm, 6 mm, 72 GPa and 2750 kg/m^3, respectively. The beam is modelled using three spectral finite elements and one throw-off element, as explained in section 2.1 and shown in Figure 2. The first longitudinal guided wave is excited by applying an axial force to the left end of the beam. The excitation consists of a 100 kHz narrow-band six-cycle sinusoidal tone burst modulated by a Hanning window, as shown in Figure 4. The measurement point is located at the centre of the beam and the guided wave response is measured until the incident pulse reflected from the free end of the beam arrives at the measurement location. Geometric and material properties of the beam are usually modelling errors in real situations. The geometric modelling error can be minimised by accurately measuring the dimensions of the beam. In this study the material modelling error is considered a possible uncertainty parameter by assuming that the Young's modulus E can vary within $\pm 5\%$ of the actual value. Measurement error is considered and simulated by applying white noise to the time-domain response of the guided wave. Without loss of generality, it is assumed that the possible damage location varies between the centre and the right end of the beam. The maximum possible damage length and depth to be considered are 50 mm and 5.9 mm, respectively.

Fourteen cases (see Table 1) of step damage are used to comprehensively study the performance of the proposed probabilistic methodology. Case A is used as a standard case to demonstrate the ability of the method to characterise damage and quantify uncertainty, and also serves as the nominal case for comparison with the results of the other cases. The effects of the measurement noise level and damage length on the damage characterisation results are investigated in Cases B1 to B3 and

C1 to C3, respectively. Cases D1 to D3 study the effect of damage depth on the uncertainties associated with the identified model parameters, and Cases E1 to E3 examine the effects of damage location, especially when the damage is close to the end of the beam. Finally, Case F is used to demonstrate the ability of the proposed probabilistic methodology in the most difficult situation in which both the damage length and the depth are small and the damage location is near the beam end.

Figure 5 shows the simulated guided wave response signals for Cases A, E2 and E3. The damage of the three cases has the same length and depth but is located at a different location along the beam. It is clear from the figure that the scatter pulse from the damage overlaps with the incident pulse reflected from the beam end when the damage is close to the end of the beam. As mentioned in section 1, most of the non-model based methods have difficulty in identifying damage in such situations because they rely on accurate baseline subtraction, which is challenging for interfering pulses.

Case A considers a damage location at 1400 mm from left end of the beam with a damage length of 30 mm and a damage depth of 1 mm. The proposed probabilistic methodology is employed to identify the damage location L_1, length L_2, depth d and Young's modulus E. Table 2 shows the predicted damage characteristics to be L_1 = 1399.99 mm, L_2 = 29.80 mm and d = 1.04 mm, which indicates that the method is able to identify all of the uncertain parameters very well. In addition to the predicted values, the proposed probabilistic methodology also quantifies the uncertainties associated with these values by calculating the posterior PDF of the set of uncertain model parameters. The normalised marginal PDF of the damage length and depth are plotted in Figure 6, which illustrates the uncertainty associated with these identified characteristics. As it is not possible to plot a figure with more than three dimensions, the marginal PDF in Figure 6 is calculated by integrating the PDF with respect to the other two identified uncertain parameters, that is, the damage location and the Young's modulus. In addition, a non-informative prior distribution is used in the Bayesian statistical framework to calculate the posterior PDF in all of the case studies, which means that no prior information is assumed and the results depend only on the set of measured data. Figure 6 shows that the PDF value drops very sharply, even for small deviations from the optimal damage length and depth, which indicates the high confidence level that can be ascribed to the predicted damage characteristics. For easier comparison of the uncertainties of different identified model parameters from different cases, the marginal cumulative distributions of the identified parameters are calculated. The solid curves in Figures 7 and 8 show the marginal cumulative distribution of the identified damage length and depth for Case A. All of the marginal cumulative distribution graphs for damage length and depth are

normalised by the corresponding true values to enable different cases to be compared. In the case studies, the normalised identified damage length or depth is the value on the horizontal axis at which the marginal cumulative probability is equal to 0.5, and the normalised error of the identified value is the horizontal distance between that point and the normalised true values $\overline{L_2} = 1$ or $\overline{d} = 1$. The slope of the curve is a measure of the uncertainty associated with the identified value, where a steeper curve means less uncertainty.

Another convenient way to quantify uncertainty is to calculate the coefficient of variation (COV), which is a normalised measure of the dispersion of a probability distribution about its mean value. The row below the identified value in Table 2 shows the COV values of the identified results. The COV is calculated by the square root of the second central moment of the estimated probability density function about its mean. The COV of the damage location (0.0086%) is very small compared with the COVs of the other model parameters. This is because the guided wave signal usually provides accurate information on the damage location based on the time it takes for the scatter pulse to arrive from the damage [28]. The COVs of the damage length and depth are 0.54% and 2.73%, respectively. The Young's modulus is identified as $E = 72.00$ GPa, which is identical to the true value. The corresponding COV value is 0.0015%. The exact identification and extremely low COV value of the identified Young's modulus result from the high sensitivity of the propagation velocity of the guided wave to the material properties, including the Young's modulus [29]. Hence, the Young's modulus can be accurately identified with only a small uncertainty.

The effect of different levels of measurement noise on the characterisation results is investigated in Cases A and B1 to B3. Cases B1 to B3 are identical to Case A except for the level of random noise superimposed on the measured time signals, which are assumed to be 2.5% for Case B1, 7.5% for Case B2 and 15% for Case B3 compared with 5% for Case A. The identified values for the uncertain parameters in these cases are summarised in Table 2. The results show that all of the identified values are close to the true values, even for Case B3 with 15% measurement noise. The identified damage location, length and depth demonstrate that, as expected, the accuracy of the damage characteristics decreases with increased measurement noise.

The normalised marginal PDF of the identified damage length and depth of Case B3 is shown in Figure 9. The axes in Figures 6 and 9 are plotted at the same scale to enable direct comparison. Figure 9 shows that the PDF value for small deviations drops more slowly from the optimal damage length and depth in any direction compared with Figure 6 (Case A). This shows that the uncertainties associated with

the identified damage length and depth are higher in Case B3 than in Case A. The marginal cumulative distribution of the damage length and depth of Cases A and B1 to B3 are plotted in Figures 7 and 8, respectively. The slopes of these curves decrease with larger percentages of measurement noise, indicating that the uncertainty of the identified damage length and depth increases. This result is confirmed by the COV values for the identified values in Table 2. The COV value of the identified damage length increases from 0.28% (in Case B1) to 1.42% (in Case B3) when the percentage measurement noise is increased from 2.5% to 15%. Similarly, the COV value of the identified damage depth increases from 1.40% (in Case B1) to 7.42% (in Case B3).

The influence of the damage length on the uncertain parameters is investigated in Cases C1 to C3. These cases have the same damage characteristics as Case A apart from the damage length L_2, which is 40 mm for Case C1, 20 mm for Case C2 and 8 mm for Case C3. The results of the damage characterisation process are summarised in Table 3, and show that all of the identified damage parameters are close to the true values, even in Case C3 which has a very small damage length (8 mm). The identified damage length of Case C3 is 7.55 mm and the damage depth is 1.03 mm. The corresponding COV values are 5.72% and 3.53%. Figures 10 and 11 provide the detailed information on and comparison of the uncertainty associated with the identified damage length and depth for Cases A and C1 to C3. Figure 10 shows that the slopes of the curves decrease with smaller damage lengths. The decrease in slope and hence increase in prediction uncertainty is most dramatic for the small damage length considered in Case C3. As is shown in Figure 10, Case C3 has also the smallest slope and hence the largest uncertainty regarding the identified damage depth, although the difference is much less pronounced than that for the damage length.

The third set of case studies investigates the effect of different damage depths. Again, Cases D1 to D3 are the same as Case A except for the damage depth, which is 2 mm for Case D1, 1.5 mm for Case D2 and 0.5 mm for Case D3 compared with 1 mm for Case A. The characterisation results and corresponding COV values are again summarised in Table 3 and illustrate how the accuracy of the identified damage depth declines as the damage depth decreases. The identified damage depth for Case D3 is 0.56 mm, which is still very close to the true value of 0.5 mm and demonstrates the robustness of the probabilistic optimisation methodology. Figures 12 and 13 show the marginal cumulative distribution of the identified damage length and depth for Cases A and D1 to D3. These figures show that the uncertainty associated with the identified damage length and depth is larger for smaller damage depths. Shallow damage results in reduced amplitudes of the scatter waves and a decrease in signal to noise ratio because the measurement noise level is the same for all cases. Thus, the indication of damage in the measured time signal is less pronounced, which leads to larger

associated uncertainties in the damage characterisation. It is worth pointing out that the trends in Figures 12 and 13 are very similar to those in Figures 7 and 8, respectively, in which different measurement noise levels are considered. An increase in measurement noise level has the same effect as a decrease in damage depth, since both decrease the signal to noise ratio and reduce the quality of the damage features in the measured time signals.

The effect of the damage location L_1 is examined in Cases E1 to E3, which are the same as Case A but with different damage locations of 1600 mm for Case E1, 1900 mm for Case E2 and 1960 mm for Case E3. The damage characterisation results with the corresponding COV values are listed in Table 3. The COV values of the identified damage length and depth for Cases A and E1-E3 are relative close, which indicates that the uncertainties of the predictions are very similar in all cases. The identified damage locations are close to the true values, and the associated uncertainties are similar in all four cases. This illustrates that the accuracy of the damage location identification is not affected by the damage location as long as there is only limited interference from the scatter wave and the reflection from the beam end. One of the reasons for this behaviour is that the first longitudinal wave mode propagates without dispersion. Hence, the scattering wave response amplitude is very similar for different damage locations and the quality of the information received at the measurement location is practically identical, which enables the determination of the arrival time of the reflected pulse from the damage with the same accuracy. However, the uncertainties of the identified damage length and depth are slightly increased for Case E3 when the damage is located relatively close to the end of the beam. This is because the scatter response is hidden in the excitation pulse reflected from the end of the beam, as shown in Figure 5.

Case F is the last and most difficult case, and considers damage that is located close to the end of the beam (L_1 = 1960 mm) and is relatively short (L_2 = 10 mm) and shallow (d = 0.5 mm). The measurement noise is assumed to be 5%. The characterisation results and the calculated COV values are summarised in Table 3. The characterisation results are close to the true values and the prediction errors are very similar to those of Case A. However, the COVs of the identified damage length and depth are significantly larger in Case F than in Case A, which reflects the larger uncertainty associated with the predicted values of Case F. Nevertheless the characterisation results are evidence of the robustness and potential of the proposed probabilistic methodology to identify laminar damage in beams.

The current numerical case studies assumed the laminar type of damage in the beam. If different types of damage are existed, the proposed methodology may need to employ other damage models. However, the type of damage can usually be

pre-determined based on the engineer's judgement, characteristic and material of the structures.

4 Conclusions

This paper introduces a probabilistic optimisation approach to detect and characterise laminar damage in beams utilising longitudinal guided wave signals measured at a single point on a beam. The proposed methodology not only determines the multivariate damage characteristics, but also quantifies the uncertainties of the predicted values, thus providing essential information for making decisions on necessary remedial work. A comprehensive series of numerical case studies is carried out using spectral finite element wave propagation modelling that considers measurement noise and material uncertainty. A two-stage optimisation process consisting of simulated annealing is implemented to guarantee that the solution finds the global optimum, followed by a standard simplex search method that maximises the probability density function of the damage scenario conditional on a set of measurements. The case study results demonstrate the potential and robustness of the method. All three damage parameters (location, length and depth) are successfully identified, even for damage located close to the end of the beam and small and shallow damage. The uncertainties associated with the predicted damage characteristics increase with higher levels of measurement noise, smaller damage lengths, smaller damage depths and increased proximity of the damage to the end of the beam. However, even in cases in which the scatter wave is completely hidden in the reflection of the interrogation pulse from the end of the beam, the predicted values only differ from the true values by less than 12%, with COVs of less than 8.5%. The proposed methodology is currently verified in experimental studies and extended to characterise multiple delaminations in composite beams.

Acknowledgements

C.T. Ng would like to acknowledge the financial support from a University of Queensland Research Scholarship (UQRS), a University of Queensland International Research Award (UQIRA), and a supplementary postgraduate scholarship from the Cooperative Research Centre for Advanced Composite Structures Limited (CRC-ACS).

References

1 Cawley P, Adams, RD. The location of defects in structures from measurements of natural frequencies. Journal of Strain Analysis for Engineering Design

1979;14:49-57.

2 Rizos PF, Aspragathos N, Dimarogonas AD. Identification of crack location and magnitude in a cantilever beam from the vibration modes. Journal of Sound and Vibration 1990;138:381-88.

3 Kim JT, Ryu YS, Cho HM, Stubbs N. Damage identification in beam-type structures: frequency-based method vs mode-shape-based method. Engineering Structures 2003;25:57-67.

4 Lam HF, Ng CT. The selection of pattern features for structural damage detection using an extended Bayesian ANN algorithm. Engineering Structures 2008; 30(10): 2762-2770.

5 Law SS, Lu ZR. Crack identification in beam from dynamic responses. Journal of Sound and Vibration 2005;285:967-87.

6 Lam HF, Ng CT, Veidt M. Experimental characterization of multiple cracks in a cantilever beam utilizing transient vibration data following a probabilistic approach. Journal of Sound and Vibration 2007;305:34-49.

7 Sohn H, Farrar CR, Hernez FM, Czarnecki JJ, Shunk DD, Stinemates DW, Nadler BR. A review of structural health monitoring literature: 1996-2001. Report No. LA-13976-MS, Los Alamos National Laboratory, Los Alamos, N.M, 2004.

8 Rose JR. A baseline and vision of ultrasonic guided wave inspection potential. Journal of Pressure Vessel technology 2002;124:273-82.

9 Raghavan A, Cesnik CES. Review of guided-wave structural health monitoring. The Shock and Vibration Digest 2007;39:91-114.

10 Jiang Z, Kabeya K, Chonan S. Longitudinal wave propagation measuring technique for structural health monitoring. Proceedings of the SPIE Conference on Smart Structures and Integrated Systems 1999;3668:343-50.

11 Krawczuk M. Application of spectral beam finite element with a crack and iterative search technique for damage detection. Finite Elements in Analysis and Design 2002;38:537-48.

12 Li Z, Xia S, Wang J, Su X. Damage detection of cracked beams based on wavelet transform. International Journal of Impact Engineering 2006;32:1190-1200.

13 Liew CK, Vedit M. Guided waves damage identification in beams with test pattern dependent series neural network systems, World Scientific and Engineering Academy and Society (WSEAS) Transactions on Signal Proceeding 2008;4:86-96.

14 Konstantinidis GK, Drinkwater BW, Wilcox PD. The temperature stability of guided wave structural health monitoring systems. Smart material and structures 2006;15:967-76.

15 Fouskakis D, Draper D. Stochastic optimization: a review. International Statistical Review 2002;70:315-49.
16 Murata T, Ishibuchi H, Tanaka H. Genetic algorithms for flowshop scheduling problems. Computers and Industrial Engineering 1996; 30(4): 1061-1071.
17 Rao SS, Xiong Y. A hybrid genetic algorithm for mixed-discrete design optimization. Journal of Mechanical Design 2005, 127(6): 1100-1112.
18 Christodoulou K, Ntotsios E, Papadimitriou C, Panetsos, P. Structural model updating and prediction variability using Pareto optimal models. Computation Methods in Applied Mechanics and Engineering 2008; 198(1): 138-14.
19 Beck JL, Katafygiotis LS. Updating models and their uncertainties I: Bayesian statistical framework. Journal of Engineering Mechanics, ASCE 1998;124:455-61.
20 Doyle JF. A spectrally formulated finite element for longitudinal wave propagation. Journal of Modal Analysis 1988;3:1-5.
21 Krawczuk M, Grabowska J, Palacz M. Longitudinal wave propagation part I – comparison of rod theories. Journal of Sound and Vibration 2006;295:461-78.
22 Papadimitriou C, Beck JL, Katafygiotis LS. Asymptotic expansions for reliability and moments of uncertain systems. Journal of Engineering Mechanics, ASCE 1997;123:1219-29.
23 Lam HF, Ng CT. A probabilistic method for the detection of obstructed cracks of beam-type structures using spatial wavelet transform. Probabilistic Engineering Mechanics 2008; 23(2-3): 237-245.
24 Lam HF, Lee YY, Sun HY, Cheng GF, Guo X. Application of the spatial wavelet transform and Bayesian approach to the crack detection of a partially obstructed beam. Thin-walled Structures 2005; 43(1): 1-21.
25 Kirkpatrik S, Gelatt CD, Vecchi MP. Optimization by simulated annealing, IBM Research Report RC 9355, 1982.
26 Lagarias JC, Reeds JA, Wright MH, Wright PE. Convergence properties of the Nelder-Mead Simplex Method in low dimensions. SIAM Journal of Optimization 1998;9:112-47.
27 Otten RHJM, van Ginneken LPPP. The Annealing Algorithm, Kluwer Academic Publishers, 1989.
28 Giurgiutiu VB, Zhao W. Piezoelectric wafer active sensor embedded ultrasonics in beams and plates. Society for Experimental Mechanics 2003;43:428-49.
29 Mossberg M, Hillstrom L, Soderstrom T. Non-parametric identification of viscoelastic materials from wave propagation experiments. Automatica 2001;37:511-21.

Figures

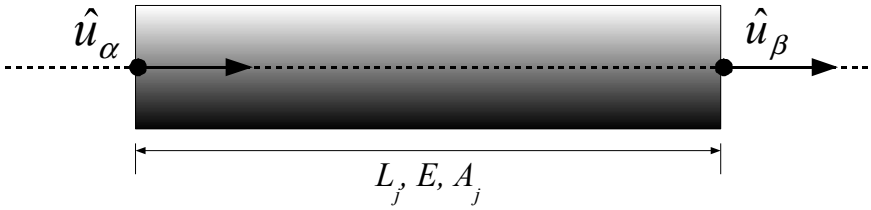

Figure 1: Spectral finite element for the fundamental longitudinal guided wave mode

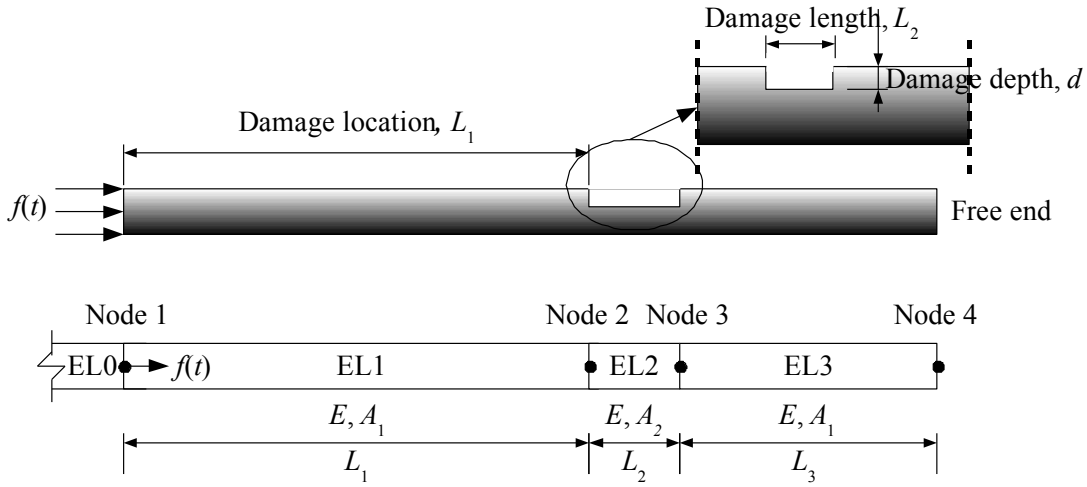

Figure 2: Semi-infinite spectral finite element model of a beam with step damage

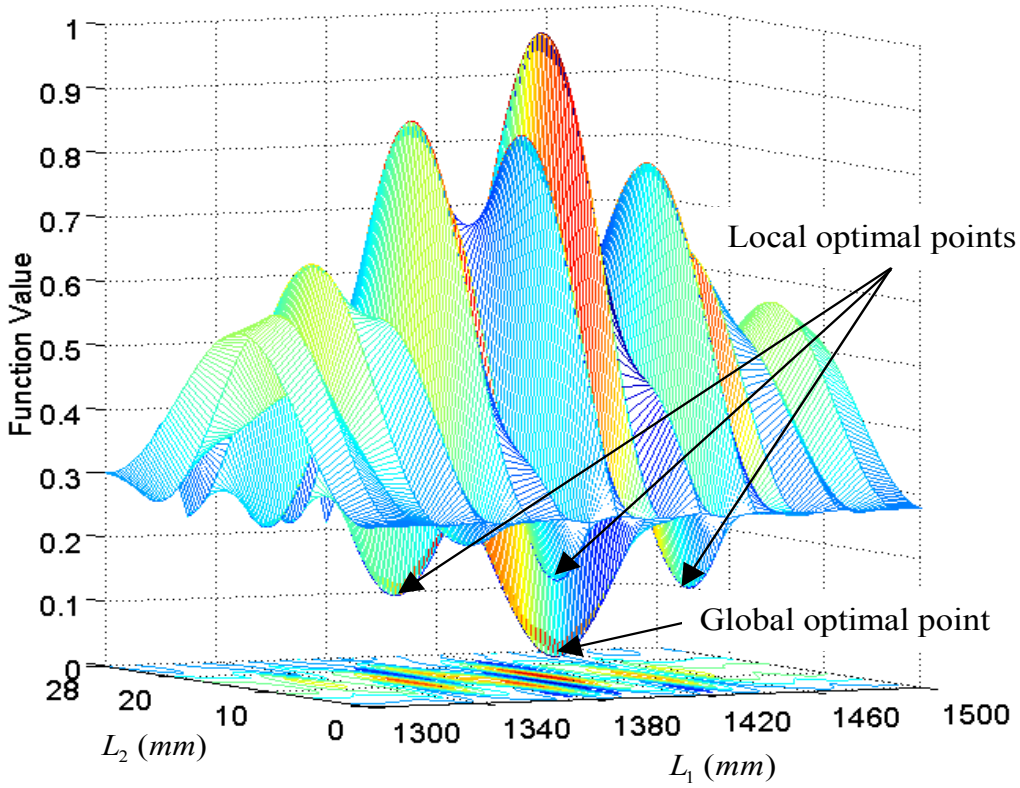

Figure 3: Typical search space of the cost function

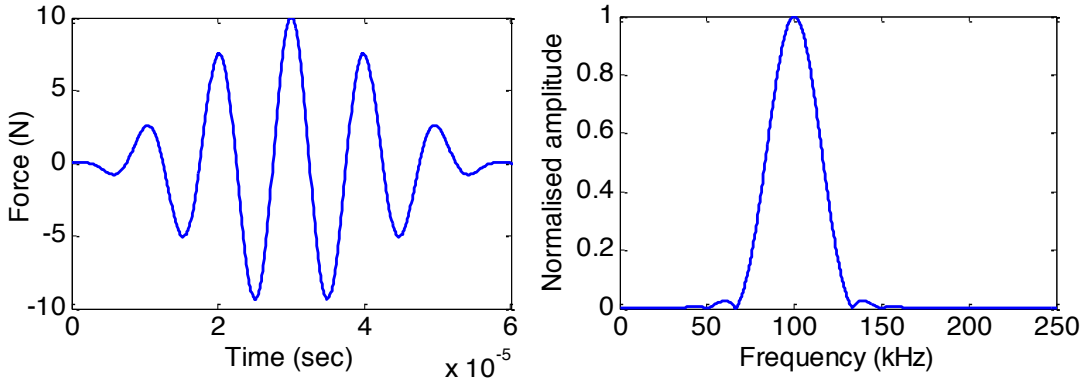

Figure 4: Six-cycle 100kHz sinusoidal excitation signal modulated by a Hanning window in time and frequency domain

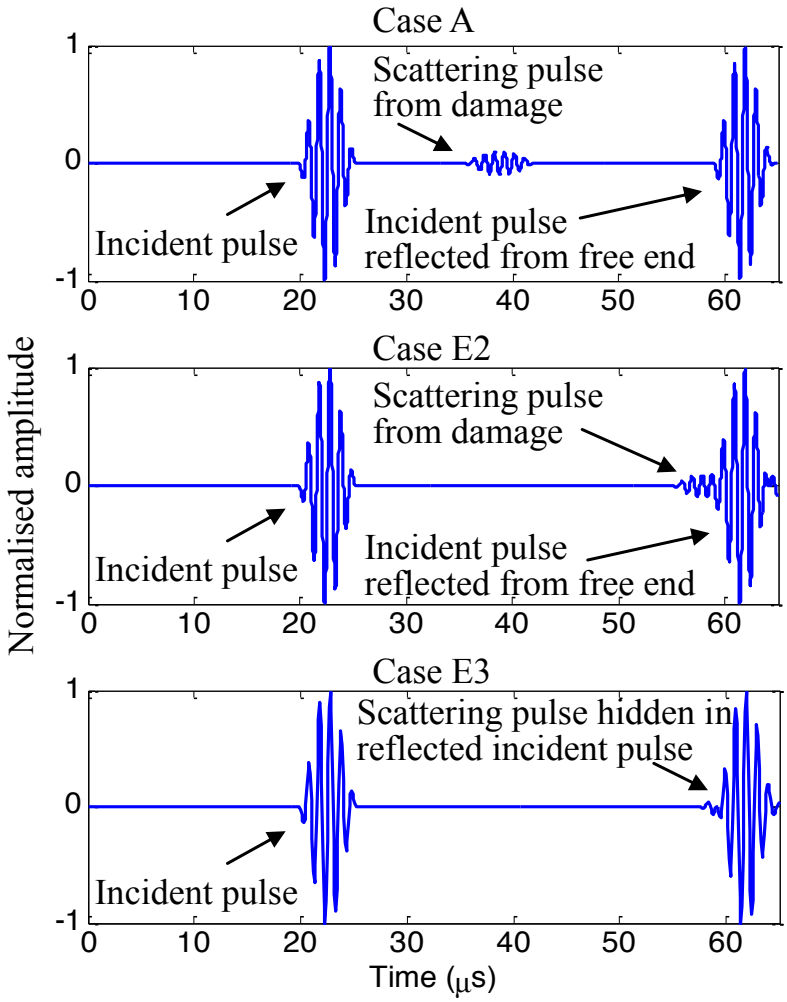

Figure 5: Simulated guided wave response at the measurement point in Cases A, E2 and E3

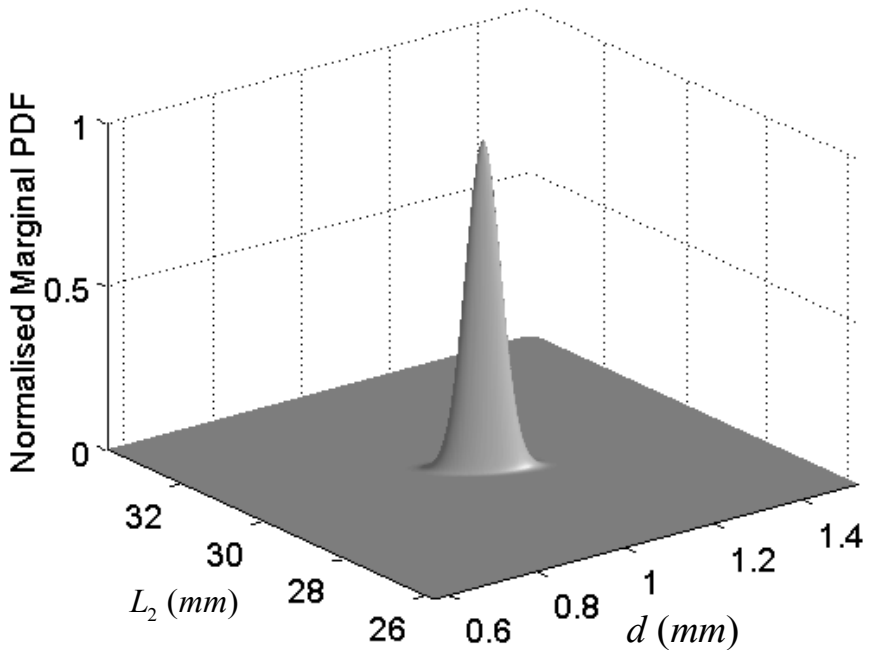

Figure 6: Normalised marginal PDF of the identified damage length (L_2) and depth (d) in Case A.

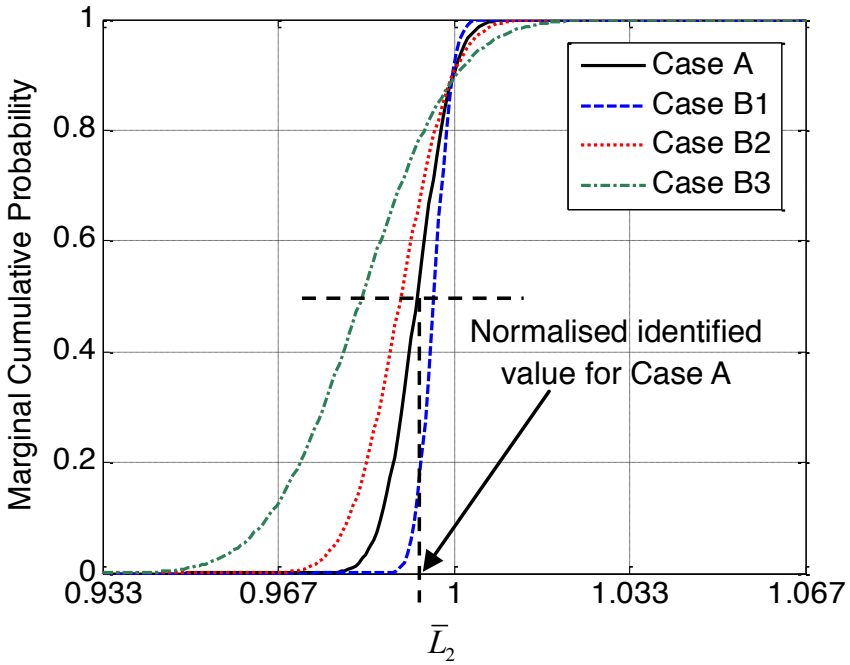

Figure 7: Marginal cumulative distribution of the normalised identified damage length ($\bar{L}_2$) in Cases A and B1-B3

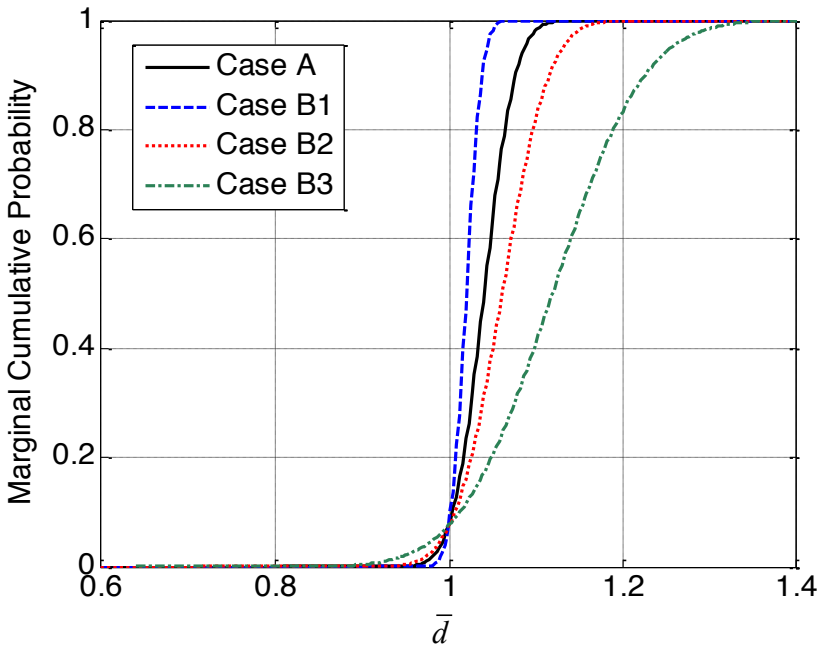

Figure 8: Marginal cumulative distribution of the normalised identified damage depth ($\bar{d}$) in Cases A and B1-B3

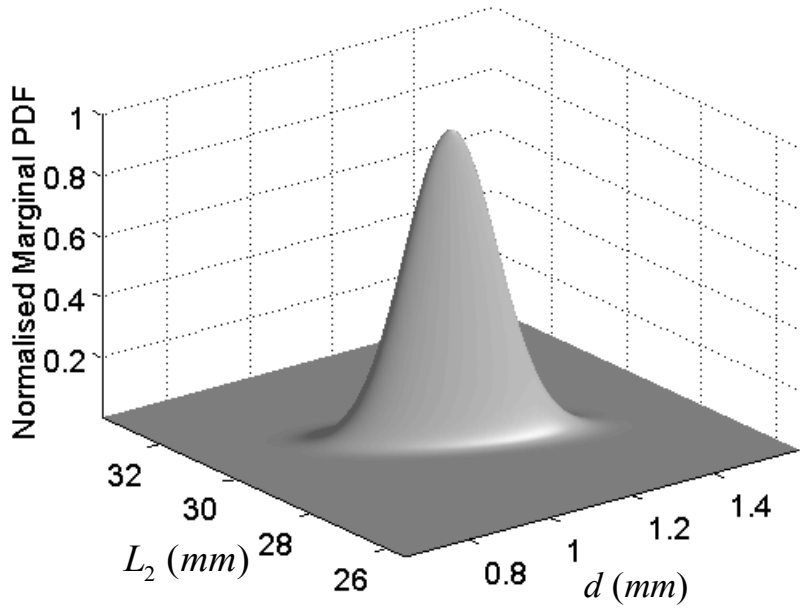

Figure 9: Normalised marginal PDF of the identified damage length (L_2) and depth (d) in Case B3

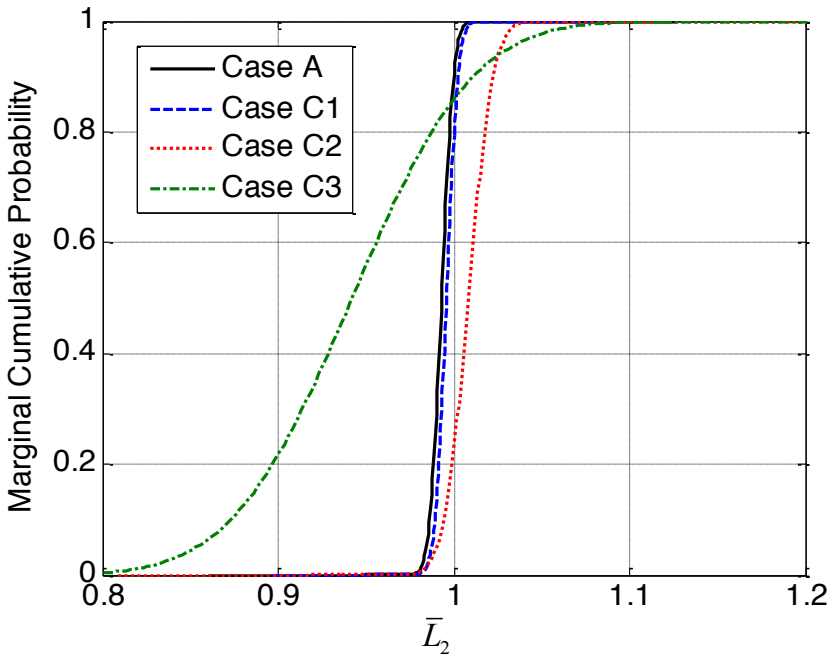

Figure 10: Marginal cumulative distribution of the normalised identified damage length ($\bar{L}_2$) in Cases A and C1-C3

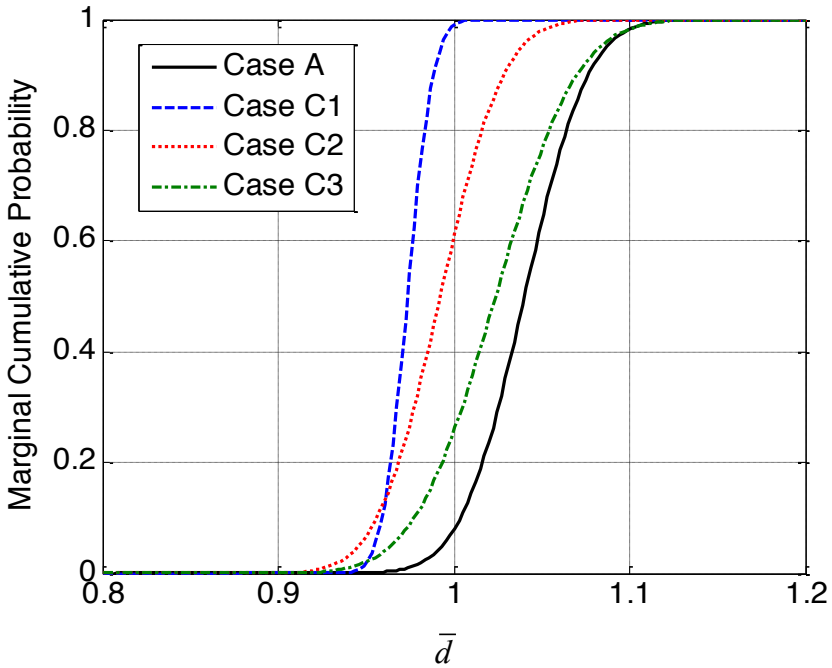

Figure 11: Marginal cumulative distribution of the normalised identified damage depth ($\bar{d}$) in Cases A and C1-C3

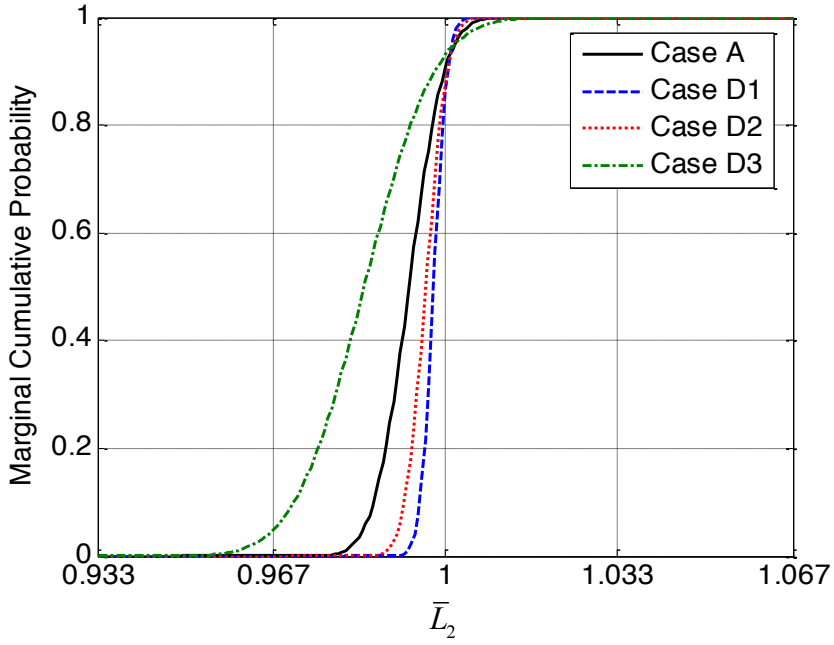

Figure 12: Marginal cumulative distribution of the normalised identified damage length ($\bar{L}_2$) in Cases A and D1-D3

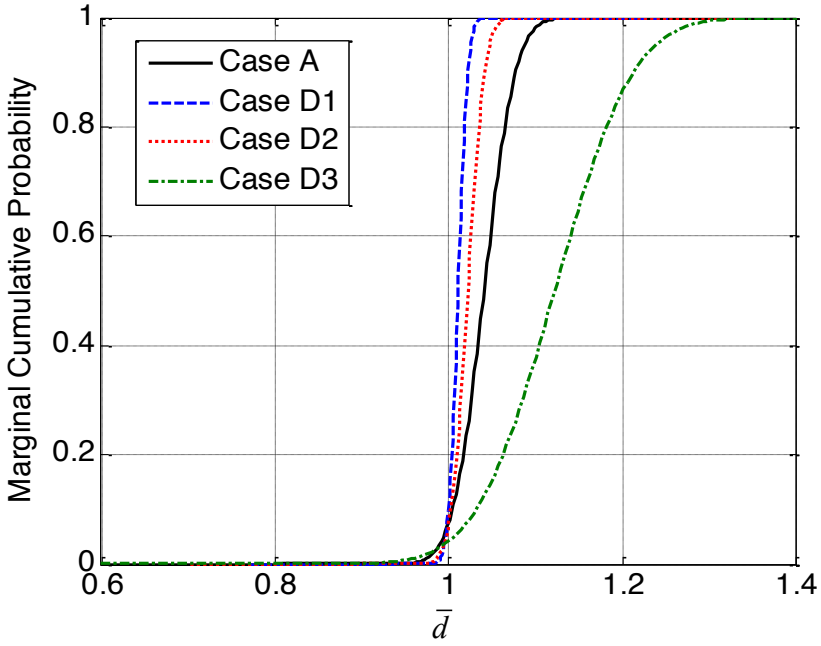

Figure 13: Marginal cumulative distribution of the normalised identified damage depth ($\bar{d}$) in Cases A and D1-D3

Tables

Table 1: Summary of all of the cases in the numerical case study

Situation	Case	L_1 (mm)	L_2 (mm)	d (mm)	Noise (%)
Standard case	A	1400	30	1	5
Different measurement noise	B1	1400	30	1	2.5
	B2	1400	30	1	7.5
	B3	1400	30	1	15
Different L_2	C1	1400	40	1	5
	C2	1400	20	1	5
	C3	1400	8	1	5
Different d	D1	1400	30	2	5
	D2	1400	30	1.5	5
	D3	1400	30	0.5	5
Different L_1	E1	1600	30	1	5
	E2	1900	30	1	5
	E3	1960	30	1	5
Combined case	F	1960	10	0.5	5

Table 2: Identified results and corresponding COVs for Cases A and B1-B3

Case		L_1 (mm)	L_2 (mm)	d (mm)	E (GPa)
	True value	1400	30	1	72
A	Identified value	**1399.99**	**29.80**	**1.04**	**72.00**
	COV (%)	*0.0086*	*0.5374*	*2.7254*	*0.0015*
B1	Identified value	**1400.00**	**29.90**	**1.02**	**72.00**
	COV (%)	*0.0044*	*0.2781*	*1.3964*	*0.0008*
B2	Identified value	**1399.98**	**29.71**	**1.06**	**72.00**
	COV (%)	*0.0127*	*0.7785*	*3.9846*	*0.0023*
B3	Identified value	**1399.96**	**29.49**	**1.12**	**72.00**
	COV (%)	*0.0243*	*1.4240*	*7.4233*	*0.0045*

Table 3: Identified results and corresponding COVs for Cases C1-C3, D1-D3, E1-E3 and F

Case		L_1 (mm)	L_2 (mm)	d (mm)	E (GPa)
	True value	1400	40	1	72
C1	Identified value	**1400.02**	**39.84**	**0.97**	**72.00**
	COV (%)	*0.0083*	*0.5196*	*1.1768*	*0.0015*
	True value	1400	20	1	72
C2	Identified value	**1399.99**	**20.18**	**0.98**	**72.00**
	COV (%)	*0.0096*	*1.0936*	*2.8457*	*0.0016*
	True value	1400	8	1	72
C3	Identified value	**1400.15**	**7.55**	**1.03**	**72.00**
	COV (%)	*0.0158*	*5.7202*	*3.5252*	*0.0020*
	True value	1400	30	2	72
D1	Identified value	**1399.97**	**29.94**	**2.02**	**72.00**
	COV (%)	*0.0036*	*0.2126*	*0.8717*	*0.0017*
	True value	1400	30	1.5	72
D2	Identified value	**1399.98**	**29.90**	**1.53**	**72.00**
	COV (%)	*0.0053*	*0.3241*	*1.4939*	*0.0016*
	True value	1400	30	0.5	72
D3	Identified value	**1400.01**	**29.54**	**0.56**	**72.00**
	COV (%)	*0.0177*	*1.0750*	*6.2842*	*0.0015*
	True value	1600	30	1	72
E1	Identified value	**1599.96**	**30.03**	**1.00**	**72.00**
	COV (%)	*0.0078*	*0.5810*	*2.8706*	*0.0015*
	True value	1900	30	1	72
E2	Identified value	**1899.70**	**30.27**	**0.95**	**72.00**
	COV (%)	*0.0066*	*0.5060*	*2.8650*	*0.0015*
	True value	1960	30	1	72
E3	Identified value	**1960.00**	**29.74**	**1.01**	**72.00**
	COV (%)	*0.0051*	*0.6352*	*3.1517*	*0.0026*
	True value	1960	10	0.5	72
F	Identified value	**1960.38**	**9.30**	**0.52**	**72.00**
	COV (%)	*0.0196*	*8.1676*	*3.8594*	*0.0025*